

Chemical Science

Accepted Manuscript

This article can be cited before page numbers have been issued, to do this please use: M. Xu, X. Fu, S. Meng, S. Gao, Y. Wang and Z. Gu, *Chem. Sci.*, 2026, DOI: 10.1039/D5SC07611K.



This is an Accepted Manuscript, which has been through the Royal Society of Chemistry peer review process and has been accepted for publication.

Accepted Manuscripts are published online shortly after acceptance, before technical editing, formatting and proof reading. Using this free service, authors can make their results available to the community, in citable form, before we publish the edited article. We will replace this Accepted Manuscript with the edited and formatted Advance Article as soon as it is available.

You can find more information about Accepted Manuscripts in the [Information for Authors](#).

Please note that technical editing may introduce minor changes to the text and/or graphics, which may alter content. The journal's standard [Terms & Conditions](#) and the [Ethical guidelines](#) still apply. In no event shall the Royal Society of Chemistry be held responsible for any errors or omissions in this Accepted Manuscript or any consequences arising from the use of any information it contains.

ARTICLE

Modulation of Nanoscale Sinuosity in Asymmetric Nano-Channel for High-Resolution Separation of Trace Xylene Isomer Impurities

Ming Xu,^{†a} Xiao-Yi Fu,^{†a} Sha-Sha Meng,^{†a} Shu-Rui Gao,^a Yu Wang^a and Zhi-Yuan Gu^{*a}Received 00th
January 20xx,
Accepted 00th January 20xx

DOI: 10.1039/x0xx00000x

The purification of para-xylene (pX) to ultra-high levels is critical for producing high-performance polyethylene terephthalate, yet trace-level quantification of its isomeric impurities, meta-xylene (mX) and ortho-xylene (oX), remains a formidable challenge due to their nearly identical boiling points and molecular dimensions. This study presented an aluminum-based metal-organic framework, Al-TCPB-Me₂, featuring asymmetric one-dimensional channels with a high sinuosity ratio that coupled molecular sieving and shape matching to achieve the baseline separation of xylene isomers. Structural characterization confirmed a sinuous channel with an entrance size of ~6.8 Å, which excluded oX while enabling selective recognition of pX over mX through asymmetric binding sites. Density functional theory calculations revealed that four methyl groups in the sinuous channel formed hydrophobic interactions with two methyl groups in pX molecules, while only three methyl groups interacted with methyl groups in mX molecules, resulting in stronger binding of pX than mX. The Al-TCPB-Me₂ column achieved high separation resolutions (24.9 for mX/pX and 31.1 for oX/pX) and successfully qualified the impurities as low as 200 ppm in the real high-quality xylene sample, surpassing all conventional columns. Comparative tests with a straight-channel Al-TCPB variant emphasized the sinuous geometry's role in enabling tandem separation mechanisms. This work establishes asymmetric sinuous channels as an effective design principle for integrating tandem molecular sieving and shape matching, offering a powerful strategy for the quantification of trace-level structurally similar impurities in real sample analysis.

Introduction

Para-xylene (pX) is a crucial precursor in the production of terephthalic acid (PTA), which is essential for manufacturing polyethylene terephthalate (PET) plastics and polyester fibers, widely used in packaging, textiles, and consumer goods.¹⁻³ The production of high-performance polyester requires ultra-high-purity pX, placing stringent demands on the detection and quantification of impurities, particularly its isomeric counterparts. Meta-xylene (mX) and ortho-xylene (oX) are the primary isomeric impurities, and even trace amounts can adversely affect the properties and performance of downstream products.⁴ However, the quantification of impurities in pX presents severe analytical challenges, which arises from the isomers' minimal boiling point variations (0.7–6.0 K) and similar molecular dimensions (pX: 5.8 Å; mX: 6.8 Å; oX: 6.8 Å).^{5,6} Conventional gas chromatography (GC) stationary phases hardly achieve xylene isomer separation due to these physicochemical similarities, leading to compromised accuracy in the quantification of pX impurities, especially the isomeric impurities at trace levels.^{7,8} This underscores the urgent need

for highly selective chromatographic stationary phases with enhanced separation efficiency and accuracy in trace impurity quantification.⁹

Metal-organic frameworks (MOFs) have emerged as promising materials for the separation of structurally similar molecules due to their precisely tunable pore environments.¹⁰⁻¹² Controlling pore architecture has enabled improved separation of aromatic isomers, alkane/alkene mixtures, electronic specialty gases, and cyclohexane/benzene azeotropes in adsorption and chromatographic systems.^{13,14} Despite these developments, current MOF-based separators remain insufficient for the analytical demands of industrial pX purification. Most reported systems focus on equimolar or simplified binary mixtures and aim to enhance adsorption selectivity under balanced laboratory conditions.¹⁵ However, industrial impurity analysis presents a fundamentally different challenge, where trace-level mX and oX must be detected in the presence of an overwhelmingly dominant pX matrix—often with concentration differences spanning several orders of magnitude. Under such extreme disparity, even MOFs with good inherent selectivity struggle because competitive adsorption from the dominant component. A fundamentally new material design paradigm is required, one capable of selective recognition of minor impurities despite intense competitive adsorption from the major component.

Classical separation mechanisms provided by MOF separators alone are insufficient to meet this requirement.¹⁶⁻²¹ Molecular sieving selectively adsorbs smaller molecules while

^a State Key Laboratory of Microbial Technology, Jiangsu Collaborative Innovation Center of Biomedical Functional Materials, Jiangsu Key Laboratory of New Power Batteries, College of Chemistry and Materials Science, School of Food Science and Pharmaceutical Engineering, Nanjing Normal University, Nanjing 210023, China

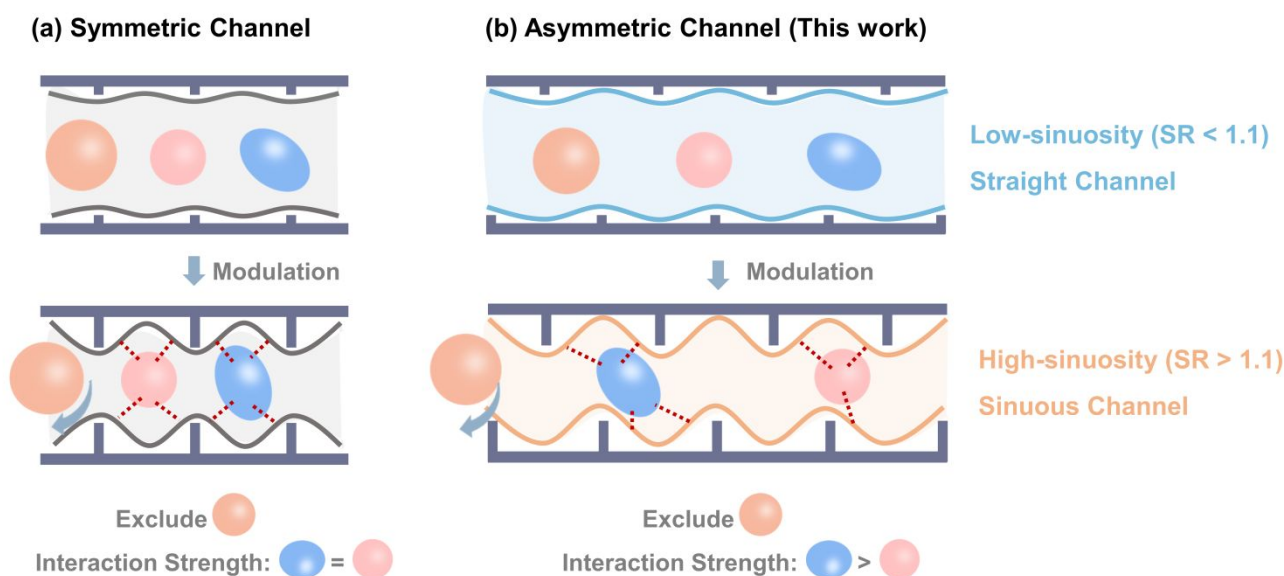
[†] These authors contributed equally to this work

Supplementary Information available: [details of any supplementary information available should be included here]. See DOI: 10.1039/x0xx00000x



excluding larger species,^{22–24} whereas shape matching relies on the geometric fit between adsorbates and pore environments to induce strong configuration-specific interactions.^{25–29} Recent studies have validated combining molecular sieving and shape matching as an efficient means to further enhance the

separation performance of MOFs.^{30–32} In practice, however, these approaches have relied predominantly on size-based sieving, while the potential of shape matching has been less fully



Scheme 1. (a) The schematics of modulating the symmetric channel to combine molecular sieving and shape matching mechanism. (b) The schematics of modulating the asymmetric channel sinuosity to combine molecular sieving and shape matching mechanisms in this work. The sinuosity ratio (SR) lower than 1.1 indicates a straight channel, while SR higher than 1.1 indicates a sinuous channel.

realized. In most cases, shape matching merely reinforces sieving or enhances adsorption capacity, rather than directly separating molecules after adsorption.^{13, 14} This limitation arises largely from the prevailing use of symmetric channel architectures, in which separation is achieved by tuning channel windows to exclude larger molecules (Scheme 1a). Such an approach makes it difficult to modify the internal cavity geometry and thus restricts the precision of shape matching.^{30, 31} From a geometric standpoint, asymmetric channels present a more versatile alternative because they are inherently sensitive to subtle differences in molecular geometry and provide greater opportunities for coupling sieving with shape recognition.^{33–35} Importantly, asymmetry can be introduced through chemical functionalization, which not only regulates channel window size but also modifies channel sinuosity, thereby enabling more precise discrimination of structural isomers (Scheme 1b). The sinuosity ratio (SR) of MOF channels can be defined analogously to the river sinuosity ratio, where SR values below 1.1 indicate straight channels and values above 1.1 indicate sinuous channels (Fig. S1). Applying this principle to the particularly demanding separation of xylene isomers requires delicate channel design, in which both asymmetry and sinuosity are finely tuned to achieve optimal molecular complementarity.

Here, to construct the asymmetric sinuous channels, the $\text{Al}(\text{OH})_2\text{O}_4$ chains with zigzag coordination mode and TCPB-Me₂ ($\text{H}_4\text{TCPB-Me}_2 = 1,2,4,5\text{-tetrakis(4-carboxyphenyl)-3,6-dimethylbenzene}$) with two additional methyl groups as constraints were chosen to coordinate in a staggered manner. It was then

developed as a high-performance stationary phase for baseline separation of trace xylene isomers from their main component through the synergistic molecular sieving and shape-matching mechanisms. The powder X-ray diffraction (PXRD) pattern and high-angle annular dark-field (HAADF) image confirmed Al-TCPB-Me₂ framework processed a *fri* topology with a one-dimensional (1D) sinuous channel (channel 1, SR = 1.14, Fig. 1) with the entrance size of approximately 6.8 Å. The oX with the largest size was excluded from channel 1 and exhibited the fastest diffusion constant among the three isomers. At the same time, the sinuous geometry resulted in asymmetric binding sites inside the channel, leading to different shape-matching effects for pX and mX. Density functional theory (DFT) simulations demonstrated that pX exhibited the strongest binding energy to the channel.^{36, 37} In detail, the alignment of the four methyl groups in the channel interacted with the two methyl groups in pX molecules, while only three methyl groups interacted with the two methyl groups in mX molecules, resulting in more negative binding energies of pX than mX. Moreover, the Al-TCPB-Me₂ stationary phase achieved the separation resolution (R_s) of 24.9 and 31.1 for mX/pX and oX/pX, respectively, which was much higher than the commercial column HP-5. Most importantly, the Al-TCPB-Me₂ column can quantify the trace mX or oX isomer impurities at concentrations as low as 200 ppm in pure pX sample. For comparison, an Al-TCPB stationary phase with straight channel 1 (SR = 1.05) was also developed.³⁸ Although the Al-TCPB demonstrated good performance in



ARTICLE

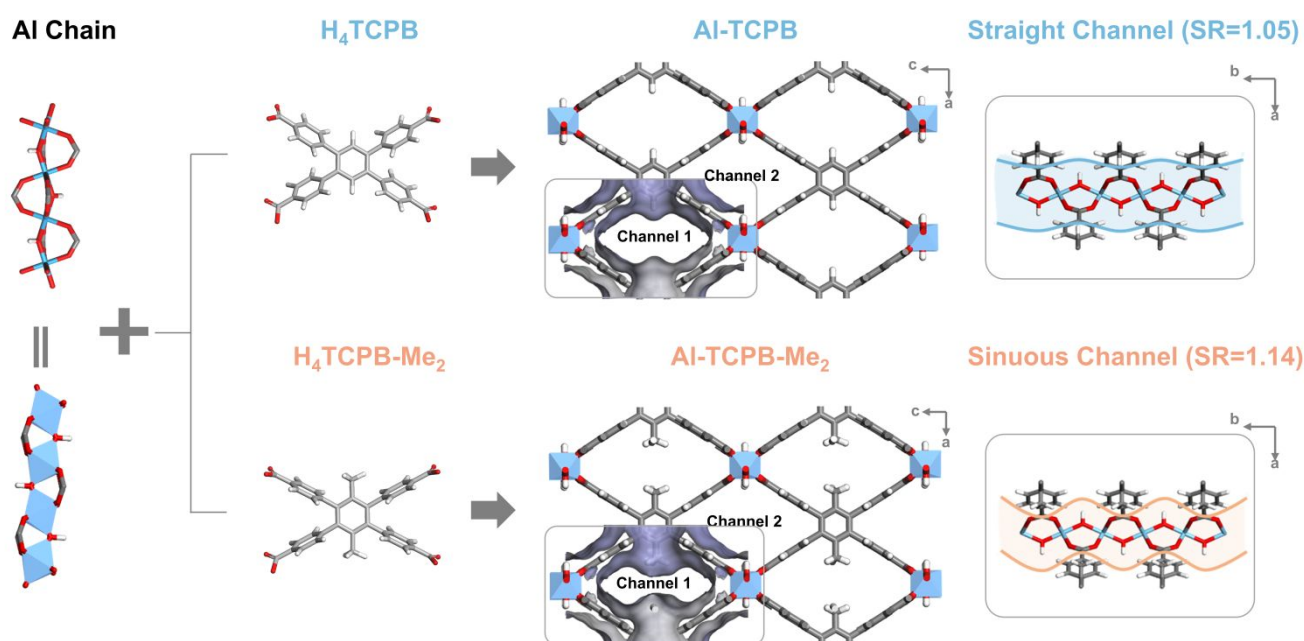


Fig. 1. Schematic illustration of isostructural Al-TCPB and Al-TCPB-Me₂ MOFs constructed by aluminium chains and H₄TCPB/H₄TCPB-Me₂ ligands. These two MOFs contain two types of channels, the sinuous/straight channel 1 and the straight channel 2. The Figs in the rightmost column highlighted the side view of channel 1 from the c-axis.

separating para-isomer from chlorotoluene and dichlorobenzene, it failed to separate meta and ortho-isomers, highlighting the crucial role of the asymmetric sinuous channel in providing tandem separation mechanisms and achieving superior separation performance. This work not only presented promising materials for the qualification of trace-level xylene impurity but also provided an effective design strategy for the development of separators with tandem separation mechanisms for challenging multi-component separations.

Results and Discussion

Synthesis and Characterization

The MOF Al-TCPB was synthesized through a one-pot method, and Al-TCPB-Me₂ was obtained by changing the ligand from H₄TCPB to H₄TCPB-Me₂ in a similar manner. The ¹H nuclear magnetic resonance (NMR) spectra proved the structures of the two ligands (Fig. S2). The reported structure data revealed that the Al-TCPB framework adopts the *fri* topology, with the 3D coordination network consisting of infinite 1D Al(OH)₂O₄ chains and tetratopic carboxylic acid ligands.³⁸ In the 1D Al(OH)₂O₄ chains, the aluminum ions exhibit an octahedral coordination

environment, with two μ₂-OH groups and four carboxyl oxygen atoms from four distinct ligands participating in the coordination. The coordinated ligands are coordinated with Al(OH)₂O₄ chains in a staggered manner along the b-axis, forming two types of 1D channels, referred to as channel 1 and channel 2 (Fig. 1). Channel 2 is a completely straight channel in which four benzene rings are oriented toward the pore interior, while channel 1 is nearly straight but exhibits slight sinuosity due to the presence of hydrogen atoms on the asymmetric organic ligands. The SR of Al-TCPB channel 1 was calculated as 1.05, confirming that it can reasonably be regarded as a straight channel in the subsequent discussion. Powder X-ray diffraction (PXRD) pattern of the synthesized Al-TCPB was recorded to confirm its structure and crystallinity. The sharp diffraction peaks of Al-TCPB showed minimal deviation from the simulated one, confirming its high crystallinity and the *fri* topology (Fig. 2a). The diffraction peaks at 5.23°, 8.00°, and 9.70° correspond to the (001), (200), and (201) planes of the Al-TCPB structure.

Although the structural data for Al-TCPB-Me₂ has not yet been reported, we hypothesized that Al-TCPB-Me₂ shared an identical topology with Al-TCPB, with the only difference being the organic ligands. The introduction of additional methyl



ARTICLE

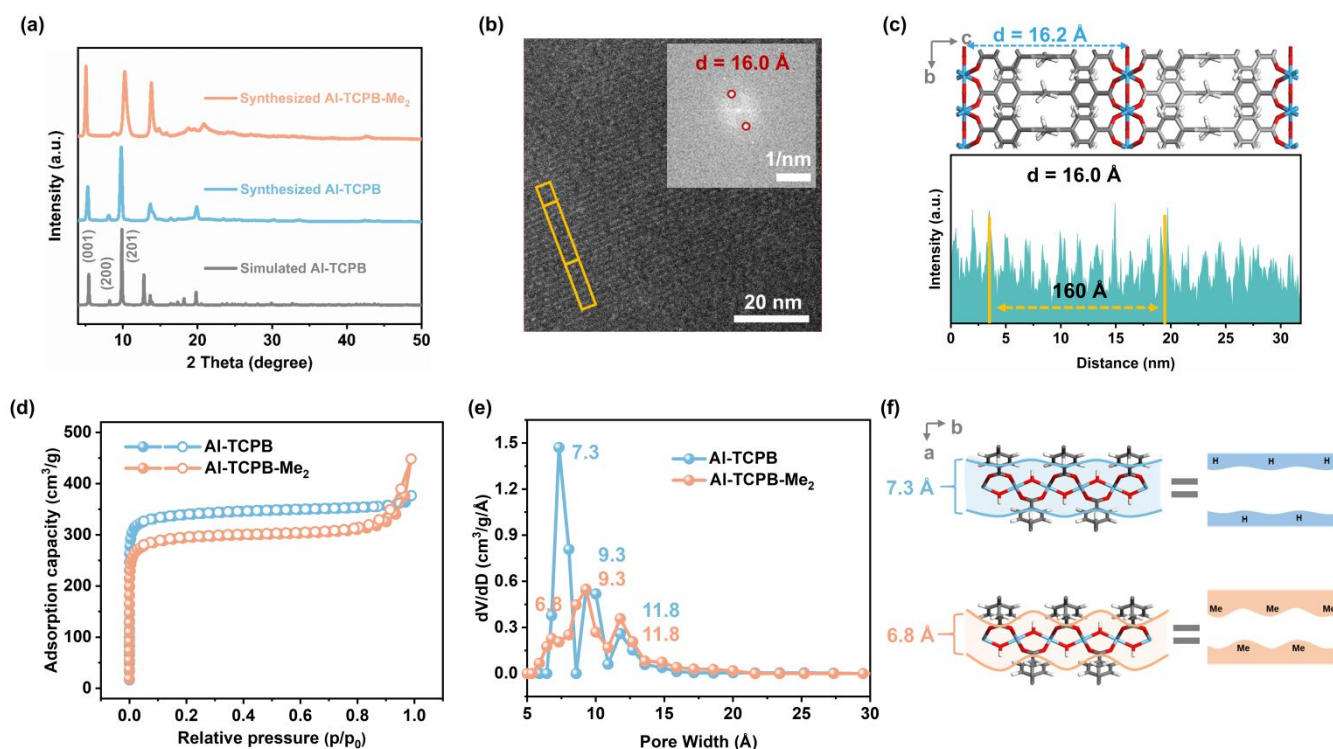


Fig. 2 (a) The PXRD patterns of Al-TCPB and Al-TCPB-Me₂. (b) The original HAADF image of Al-TCPB-Me₂. The insert is an FFT pattern. The d-spacing of two diffraction points was measured as 16.0 Å. (c) The structure of Al-TCPB-Me₂ viewed from the a-axis and the intensity profile along the orange area in (b). (d) The N₂ adsorption-desorption isotherms and (e) the pore size distributions for Al-TCPB and Al-TCPB-Me₂. (f) Channel size comparison between Al-TCPB and Al-TCPB-Me₂.

groups as constraints increases the sinuosity of channel 1 as well as functionalizes the asymmetric methyl sites (Fig. 1). Consequently, the SR of channel 1 rises from 1.05 to 1.14, indicating the formation of an asymmetric sinuous channel in Al-TCPB-Me₂. The solid-state ¹³C NMR spectra proved the presence of the two methyl groups at the synthesized Al-TCPB-Me₂ (Fig. S3). The Al-TCPB-Me₂ exhibited almost identical PXRD patterns compared with those of the simulated Al-TCPB, supporting their structural similarity. Notably, the diffraction peak for the (200) plane shifted from 8.00° to 9.29°, likely due to the introduction of the methyl groups, which reduced the interplanar spacing.^{39, 40} Furthermore, the diffraction peaks of Al-TCPB-Me₂ were broader compared to those of the synthesized Al-TCPB, suggesting relatively lower crystallinity.^{41, 42}

The scanning electron microscopy (SEM) images showed that Al-TCPB-Me₂ possessed nanoplate morphology (Fig. S4). In order to investigate the topology of Al-TCPB-Me₂, high-angle annular dark-field (HAADF) imaging was performed. The HAADF images revealed distinct lattice fringes (Fig. 2b), in which the Al chains were distinguishable as white lines against the

background and other nonmetallic atoms. The simulated structure of Al-TCPB-Me₂ from a-axis indicated that the interspacing between Al chains was 16.2 Å (Fig. 2c). The intensity profiles along the highlighted orange area in the HAADF image exhibited the spacing of 16.0 Å between Al chains, which coincides with the simulated interplanar spacing of the (001) plane. In addition, the calculated d-spacing of two adjacent points in the fast Fourier transform (FFT) pattern was also 16.0 Å, which was consistent with the interplanar spacing (16.2 Å) of the (001) plane. The above experimental findings further confirmed that Al-TCPB-Me₂ has the same structure as Al-TCPB.

The N₂ adsorption was employed to analyze the pore structures of the two Al-MOFs (Fig. 2d). Both materials displayed type-I isotherms and steep slopes at ultra-low pressures, indicating the presence of intrinsic micropores and a strong binding affinity between N₂ molecules and the MOF channels. The N₂ adsorption capacity (*p/p*₀=0.8) of Al-TCPB-Me₂ (312 cm³/g) was slightly lower than that of Al-TCPB (353 cm³/g). Similarly, the BET surface area of Al-TCPB-Me₂ (1141 m²/g) was smaller than that of Al-TCPB (1331 m²/g). These differences



ARTICLE

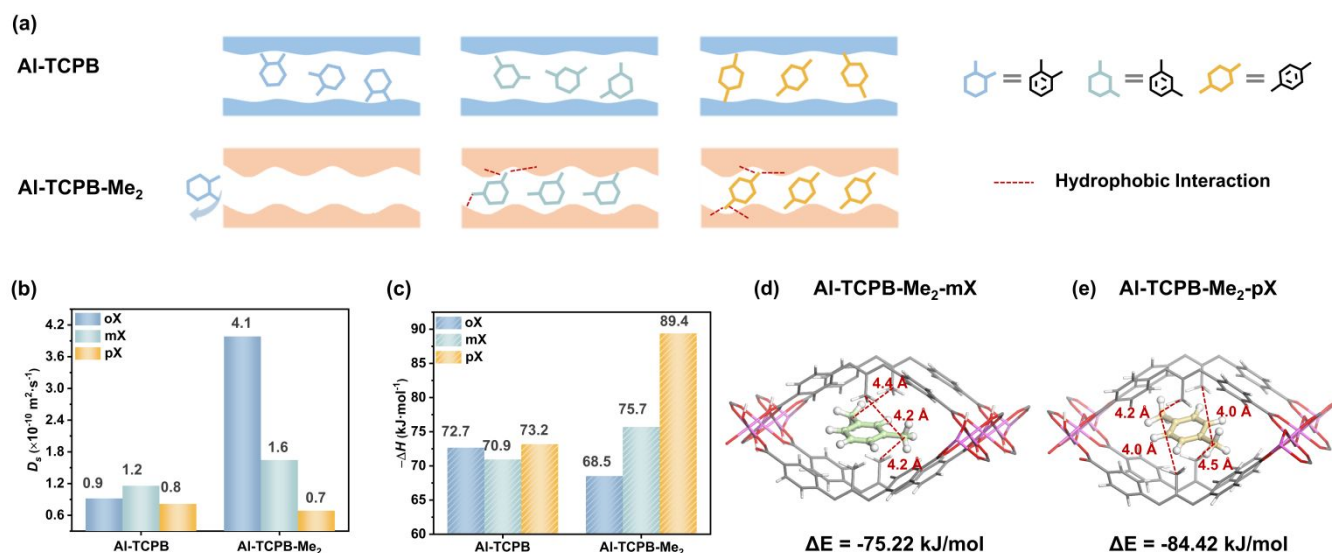


Fig. 3 (a) Schematic diagrams of oX, mX, and pX molecules transport through the asymmetric sinuous channel 1 of Al-TCPB and Al-TCPB-Me₂, respectively. (b) The experimental D_s values of oX, mX, and pX on Al-TCPB and Al-TCPB-Me₂, respectively. (c) The experimental $-\Delta H$ of oX, mX, and pX on Al-TCPB and Al-TCPB-Me₂, respectively. The DFT calculated locations of (d) mX and (e) pX within the zigzag pore of Al-TCPB-Me₂, showing the distinguished binding sites and interactions.

were attributed to the introduction of asymmetric methyl groups, which slightly changed the pore structure and hindered the N₂ adsorption. The pore size distribution, calculated using the H-K (Saito-Foley) method, revealed that both Al-MOFs contained three distinct pores (Fig. 2e). The Al-TCPB and Al-TCPB-Me₂ each had two types of pores with similar dimensions of 9.3 Å and 11.8 Å, respectively (Table S1). The smallest pore size shifted from 7.3 Å in Al-TCPB to 6.8 Å in Al-TCPB-Me₂, with a noticeable reduction in the proportion of the smallest pores in Al-TCPB-Me₂ (Fig. 2f). These observations further indicated that the introduction of the asymmetric methyl groups in the ligand partially reduced the pore volume, forming the sinuous channel with a reduction in the size of channel 1. However, the remaining channel 2 was not affected due to the similarity in topology.

The thermal stability of Al-TCPB and Al-TCPB-Me₂ was evaluated by thermogravimetric analysis (TGA) under an oxygen atmosphere (Fig. S5). The results showed that due to differing amounts of residual solvent in the materials, the mass loss of Al-TCPB and Al-TCPB-Me₂ before 250 °C was 5.60% and 3.64%, respectively. The sinuous channel of Al-TCPB-Me₂ adsorbed less residual solvent compared to the straight channel of Al-TCPB. Both host frameworks maintained structural integrity up to 425 °C, indicating the high thermostability of the two Al-MOFs. This stability can be attributed to the strong aluminum-oxygen (Al-O) bonds and the stable coordination between the Al³⁺ center and the carboxylate ligands.

Molecular Sieving Provided by the Asymmetric Sinuous Channel

After the successful synthesis of the two Al-MOFs with distinct channel architectures, they were measured in the inverse GC using xylene isomers as model analytes to evaluate the molecular sieving capabilities for isomer differentiation. The SEM images of the MOF-coated 15-meter columns from the cross-sectional view revealed that the dynamic coating process and temperature programming did not affect the morphology of MOFs (Fig. S6). Then, the kinetic parameters, including diffusion constants (D_s) and mass transfer coefficients (C -term) at 230 °C, were calculated for the comparison between Al-TCPB and Al-TCPB-Me₂. Notably, the D_s values and C -terms for oX, mX, and pX showed minimal differences when tested with the Al-TCPB coated column. Similar D_s values and C -terms indicated that Al-TCPB cannot provide molecular sieving to distinguish these isomers. The smallest pore window of Al-TCPB is 7.3 Å, which is still larger than all the xylene isomers, meaning all the xylene isomers can enter channel 1 and channel 2 of Al-TCPB, resulting in no sieving effect.

When it came to Al-TCPB-Me₂, the phenomenon had changed. The pX with the smallest kinetic diameter clearly exhibited the smallest D_s and the largest C -terms in the Al-TCPB-Me₂ coated column, indicating the slowest diffusion of pX in Al-TCPB-Me₂. This suggested that, unlike Al-TCPB, Al-TCPB-Me₂, with its smallest pore window of 6.8 Å, is able to provide the



molecular sieving effect, allowing the smallest pX to get into channel 1 while excluding larger isomers. Interestingly, oX and mX, which have almost identical kinetic diameters, displayed significantly different diffusion behaviors in Al-TCPB-Me₂. The D_s value for oX was 2.4 times higher than that for mX, indicating that most oX molecules likely diffused through the stationary phase without entering the smallest channel 1 (Fig. S7, Table S2). This behavior resulted from the unique sinuous shape of channel 1. The sinuous channel provided a tilted entrance for meta-position mX molecules, while the methyl group positioned at the channel entrance imposes additional steric hindrance on oX molecules with ortho-positioned dual methyl groups. During the fast adsorption and desorption processes, the large diffusion barrier prevented most oX molecules from entering channel 1, leading to molecular exclusion. Notably, this molecular exclusion of oX was weakened during adsorption at thermodynamic equilibrium. Single-component vapor adsorption experiments revealed that oX exhibited a slightly higher adsorption capacity in Al-TCPB-Me₂ under saturated conditions, suggesting that oX was also able to access channel 1 at high molecular concentrations (Fig. S8). The equilibrium adsorption experiments allowed molecules sufficient time to explore accessible pore spaces. Under these conditions, oX might occupy the local adsorption pockets, and its adjacent methyl groups provided a larger hydrophobic contact area, resulting in slightly higher equilibrium uptake than mX. It was worth noting that since channel 2 of both Al-TCPB and Al-TCPB-Me₂ is identical and larger than all the xylene isomers, the differing mass transfer behavior of isomers was primarily attributed to the shape of channel 1.

Shape Matching by the Asymmetric Sinuous Channel

To further investigate the shape-matching effects provided by the two Al-MOFs, the enthalpy of adsorption (ΔH), entropy of adsorption (ΔS), and Gibbs free energy of adsorption (ΔG) for xylene isomers were calculated. As shown in Fig. S9, the van't Hoff plot exhibited a linear relationship, indicating that the interaction mechanism between the MOFs and adsorbates remained consistent across the temperature range.

For Al-TCPB, the ΔH values followed the order $mX > oX > pX$ ($-70.9 > -72.7 > -73.2$ kJ/mol, Table S3). The pX exhibited the most negative ΔH value when tested with the Al-TCPB coated column, although the differences were not pronounced. Thus, the pX, with the longest molecular length, was able to interact synergistically with both channel walls, leading to a stronger affinity for Al-TCPB. In contrast, oX, with two methyl groups in adjacent positions, was reported to interact simultaneously with the metal chains, resulting in intermediate interactions with the backbone.⁴³ The shape of mX allowed it to use only one of its two methyl groups to interact with the channel wall, leading to the weakest interaction. These results suggested that Al-TCPB with low SR can provide a shape-matching effect to distinguish the thermodynamic differences between the three xylene isomers, although this effect was not significant.

For Al-TCPB-Me₂, the ΔH values for Al-TCPB-Me₂ followed the order $oX > mX > pX$ ($-68.5 > -75.7 > -89.4$ kJ/mol). The difference in ΔH values was much more significant, indicating

that Al-TCPB-Me₂ offered greater distinguishability than Al-TCPB. Notably, the ΔH value for oX in Al-TCPB-Me₂ was less negative than in Al-TCPB, and also less negative than pX and mX in Al-TCPB-Me₂, further supporting the speculation that oX molecules were predominantly excluded by the sinuous channel 1, preventing them from accessing the adsorption sites within the channel 1. The ΔH values for pX were much higher than those for mX, suggesting a stronger interaction between pX and Al-TCPB-Me₂. We supposed that the high sinuosity introduced by asymmetric methyl groups enhances shape matching effect, thereby amplifying the geometric distinctions among xylene isomers. Within the sinuous channels, the methyl groups can closely interact with the linear pX molecules, forming the strongest interaction. In contrast, mX molecules with meta-positioned methyl groups were unable to form the same interactions, resulting in a weaker interaction. The ΔS and ΔG values for the three isomers on Al-TCPB-Me₂ further supported this hypothesis (Table S3). These results proved that the sinuous channels of Al-TCPB-Me₂ can provide an effective shape-matching effect to distinguish isomers.

To test the above hypothesis, density functional theory (DFT) simulations, conducted using VASP software, were employed to further explore the shape-matching phenomena between pX and mX within the asymmetric sinuous channel 1 of Al-TCPB-Me₂ (see Supplementary Information for details). The adsorption positions of pX and mX molecules within the channel were optimized to minimize the binding energy before the comparison. The final calculated binding energies for pX and mX were -84.42 kJ/mol and -75.22 kJ/mol, respectively. The observed trend in binding energies aligned with the experimental ΔH values obtained from the inverse GC method. As illustrated in Figs 3b and 3e, both pX and mX could form C-H $\cdots\pi$ interactions with the Al-TCPB-Me₂ framework. However, the dual methyl groups of linear pX were in closer proximity to the four methyl groups of the organic ligands, resulting in a more complete hydrophobic contact between its two methyl groups and the densely methyl-decorated channel walls, which maximized dispersive interactions. In contrast, the mX molecule is shorter, and its meta-positioned methyl groups interacted with only three methyl groups of the organic ligands, leading to an incomplete overlap with these hydrophobic regions. Thus, the asymmetric sinuous channel amplifies the difference in accessible hydrophobic surface area among isomers, directly translating geometric mismatches into measurable binding energy differences. The DFT further proved that the asymmetric sinuous channels of Al-TCPB-Me₂ can provide the shape-matching effect to distinguish pX and mX.

Separation Performance of Asymmetric Sinuous Channel in Al-MOFs

Following the confirmation of the asymmetric sinuous channel's capacity for tandem molecular sieving and shape-matching effects in isomer discrimination, the Al-TCPB-Me₂ material was implemented as a GC stationary phase for isomer separation. Comparative Al-TCPB coated columns and commercial HP-5 columns were tested to separate identical isomer mixtures (Fig. 4 and Fig. S10-13).



ARTICLE

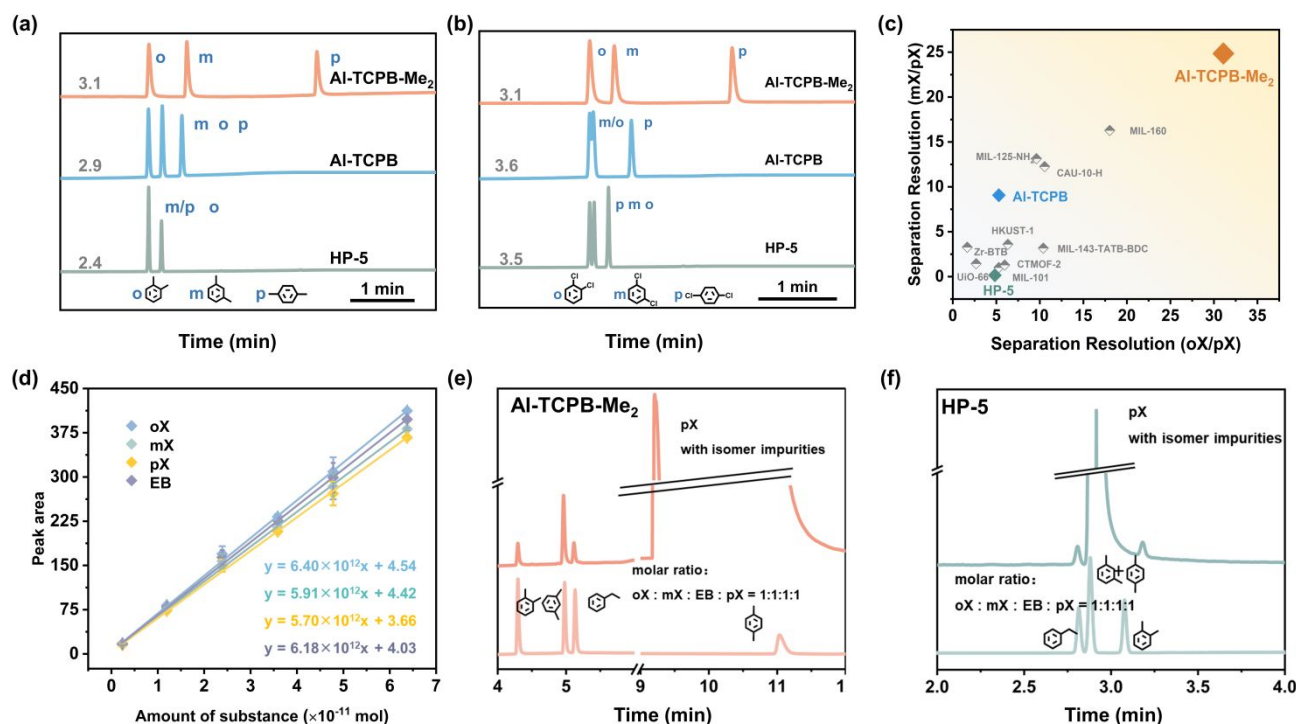


Fig. 4 The GC separation chromatograms of (a) xylene isomers and (b) dichlorobenzene isomers on HP-5, Al-TCPB, and Al-TCPB-Me₂ columns, respectively. (c) The isomer separation resolution of mX/pX and oX/pX on different MOF columns and the commercial column HP-5, respectively. (d) The standard curves of oX, mX, pX, and EB on the 30-m Al-TCPB-Me₂ column, respectively. (e) Gas chromatograms of pX with isomer impurities on the 30-m Al-TCPB-Me₂ coated column. All four isomers were totally separated from each other. (f) Gas chromatograms of pX with isomer impurities on the 30-m HP-5 column. The mX could not be separated from the main peak pX, while the peak tailing affects the accurate quantification of oX.

The concentrations of coating material were controlled as 1 mg/mL (1mL) respectively for each column, respectively, to avoid the influence (Fig. S13). Experimental results revealed that the Al-TCPB-Me₂ column achieved baseline resolution for 10 groups of disubstituted benzene isomers and alkane compounds, demonstrating superior analytical scope and separation efficiency. For xylene isomer separation, R_s values reached 24.9 (mX/pX) and 31.1 (oX/pX), significantly outperforming state-of-the-art HP-5 columns and most of the reported stationary phases (Fig. 4c and Table S4). The elution sequence (oX > mX > pX) reflected differential molecular interactions. The oX's early elution aligned with the rapid kinetic diffusion through molecular sieves, while the delayed elution of pX corresponded to the enhanced thermodynamic binding through shape matching. This tandem mechanism facilitated consistent baseline separation across various disubstituted benzene isomers, confirming the strategic advantage of engineered sinuous channels in the synergistic size exclusion and molecular recognition for ortho-, meta-, and para-isomer differentiation (Fig. 4a and Fig. S11). The column also exhibited

excellent operational and long-term stability, as confirmed by its consistent performance across multiple batches, repeated injections, thermal cycling, and seven-month storage (Fig. S14-17).

The separation performance of Al-TCPB with straight channels was also evaluated. The Al-TCPB coated column baseline separated several isomers, such as xylene and ethyltoluene, although the separation performance was significantly lower than the Al-TCPB-Me₂ coated column. For example, the R_s of oX/pX and mX/pX were 5.3 and 9.1, respectively (Table S4). Notably, the elution order of xylenes on Al-TCPB was mX > oX > pX, differing from that observed in Al-TCPB-Me₂. This elution sequence was consistent with the relative ΔH values, suggesting that the separation in Al-TCPB was primarily governed by shape-matching interactions without significant molecular sieving effects. The column efficiency of these two columns was measured by using oX as the target (Fig. S18). The column efficiency of the Al-TCPB coated column was 1895 plates/m, smaller than that of the Al-TCPB-Me₂ coated column (3289 plates/m, Table S5). When separating



chlorotoluene isomers and dichlorobenzene isomers, the Al-TCPB can separate para-isomers from others but cannot distinguish the meta- and ortho-isomers (Fig. 4b and Fig. S10). These comparative results conclusively validate the superior performance of the asymmetric sinuous channel in Al-TCPB-Me₂ with a tandem separation mechanism.

Quantification of Isomer Impurities in High Quality Sample

To assess the quantification ability of the Al-TCPB-Me₂ column, four xylene isomers (oX, mX, pX, and EB) were mixed in n-heptane at a 1:1:1:1 molar ratio. Their concentrations were adjusted by varying the volume of n-heptane. The solutions of each concentration were injected into the 30-meter Al-TCPB-Me₂ column under the same programmed heating conditions, respectively. Chromatograms showed baseline separation of all isomers with no interference in peak area integration (Fig. S19). Each isomer's calibration curve had a goodness of fit above 0.99 (Fig. 4d and Table S6). Detection limits (LODs, S/N=3) were 2.59±0.22 pg for oX, 3.11±0.22 pg for mX, 15.39±1.99 pg for pX, and 3.08±0.13 pg for EB (Table S7). It was worth noting that the above LODs could be even lower with proper analytical strategies, such as sample preparation and mass spectrometry (MS) or MS/MS detectors. These results confirmed the Al-TCPB-Me₂ column's reliable quantification performance.

To further confirm the Al-TCPB-Me₂ column's ability to quantify trace isomeric impurities, a real high-quality pX sample was analyzed. The three impurities (oX, mX, and EB) eluted between 4-6 minutes, while pure pX eluted after 12 minutes, ensuring the main pX peak broadening and trailing did not interfere with the impurity detection (Fig. 4e). Using calibration curves, the impurities of oX, mX, and EB were measured as 200±30 ppm, 800±10 ppm, and 200±20 ppm (w/w), respectively (Table S8) in the pure pX sample. It was worth noting that this sample is not aligned with the LODs for the Al-TCPB-Me₂ column. Theoretically, impurities as low as 6.3 ppm could be quantified, which is suitable for the analysis of ultrahigh-grade samples, such as electronic chemicals (>99.9994% w/w). For comparison, the conventional HP-5 column was used to analyze the same pX sample, but failed to quantify impurities due to poor separation and interference from pX peak tailing (Fig. 4f and Fig. S20). This validates the Al-TCPB-Me₂ column's superior performance in trace isomer impurity quantification.

Conclusions

In summary, we demonstrated the successful development of the Al-TCPB-Me₂ with asymmetric sinuous one-dimensional channels as a high-performance GC stationary phase for resolving persistent challenges in pX trace isomer separation and qualification. By synergistically integrating molecular sieving and shape matching mechanisms, the material's unique asymmetric sinuous channel architecture enabled oX exclusion through size selectivity while leveraging asymmetric binding interactions to differentiate pX and mX. The separation mechanism was proved by both thermodynamic interaction and kinetic diffusion investigation. The Al-TCPB-Me₂ column achieved exceptional separation resolutions and impurity

quantification down to 200 ppm in a high-purity sample, significantly surpassing conventional columns. The comparison material Al-TCPB with straight channels showed lower separation resolution of all the isomer mixtures than Al-TCPB-Me₂, emphasizing the critical role of the sinuous geometry in achieving the high performance. These findings advanced the precision of industrial xylene isomer analysis and established a versatile design strategy for engineering advanced separation materials targeting complex multi-component systems with near-identical physicochemical properties.

Author contributions

Z.-Y.G. conceived the idea and supervised the research. M.X., X.Y.F. and S.-S.M. performed the synthesis, characterization, and GC experiments and discussed the results. S.R.G. and Y.W. performed the DFT simulation. Z.-Y.G., and M. X. discussed the experimental data and wrote the paper. All authors have approved the final version of the manuscript.

Conflicts of interest

There are no conflicts to declare.

Data availability

The data supporting this article have been included as part of the Supplementary Information.

Acknowledgements

This work is supported by the National Natural Science Foundation of China (22374077 and 22474059), and the Priority Academic Program Development of Jiangsu Higher Education Institutions. This work is carried out with the support of BL17B1 at the Shanghai Synchrotron Radiation Facility (proposal 2023-NFPS-PT-500772).

Notes and references

1. Y. Liu, C. Wang, Q. Yang, Q. Ren and Z. Bao, *Coord. Chem. Rev.*, 2025, **523**, 216229.
2. M. Xu, W.-Q. Tang, S.-S. Meng and Z.-Y. Gu, *Chem. Soc. Rev.*, 2025, **54**, 1613-1633.
3. M. Rahmani, C. R. M. O. Matos, S.-Q. Wang, A. A. Bezrukov, A. C. Eaby, D. Sensharma, Y. Hjej-Andaloussi, M. Vandichel and M. J. Zaworotko, *J. Am. Chem. Soc.*, 2023, **145**, 27316-27324.
4. L. Yu, J. Zhang, S. Ullah, J. Yao, H. Luo, J. Huang, Q. Xia, T. Thonhauser, J. Li and H. Wang, *Angew. Chem. Int. Ed.*, 2023, **62**, e202310672.
5. N. Zhu, J. Wu and D. Zhao, *ACS Nano*, 2025, **19**, 2029-2046.
6. Y.-J. Zhao, W.-Q. Tang, X.-W. Wang, H.-F. Zhao, Z.-Y. Gu, Q. Yang and D. Liu, *Chem. Sci.*, 2022, **13**, 11896-11903.
7. S. Halder, Z. Xie, M. H. Nantz and X.-A. Fu, *J. Chromatogr. A*, 2022, **1673**, 463083.



8. B. Chen, C. Liang, J. Yang, D. S. Contreras, Y. L. Clancy, E. B. Lobkovsky, O. M. Yaghi and S. Dai, *Angew. Chem. Int. Ed.*, 2006, **45**, 1390-1393.
9. J. Wang, X. Lu, Z. Zhang, R. Gao, C. Pei and H. Wang, *J. Chromatogr. A*, 2024, **1718**, 464718.
10. M. Chang, Z. Wang, R. Wang, M. Liu, Y. Wang and D. Liu, *Angew. Chem. Int. Ed.*, 2025, DOI: 10.1002/anie.202515496
11. Z.-H. Guo, L.-Q. Yang, Q.-G. Zhai, G.-P. Yang and Y.-Y. Wang, *Angew. Chem. Int. Ed.*, 2025, DOI: 10.1002/anie.202519278.
12. C.-X. Chen, X. Cui, Y.-Y. Xiong, P. C. Lan, K. Tan, Z.-W. Wei, Z. Niu, C. Shan, L. Yang, S. Ma and C.-Y. Su, *Nat. Synth.*, 2025, DOI: 10.1038/s44160-025-00911-7.
13. Y. Wang, N.-Y. Huang, X.-W. Zhang, H. He, R.-K. Huang, Z.-M. Ye, Y. Li, D.-D. Zhou, P.-Q. Liao, X.-M. Chen and J.-P. Zhang, *Angew. Chem. Int. Ed.*, 2019, **58**, 7692-7696.
14. Q. Ding, Z. Zhang, C. Yu, P. Zhang, J. Wang, X. Cui, C.-H. He, S. Deng and H. Xing, *Sci. Adv.*, 2025, **6**, eaaz4322.
15. S. Lee, A. Sharma, J. H. Lee, J. Lim, S. K. Min, H. Chun and M. S. Lah, *Angew. Chem. Int. Ed.*, 2025, **64**, e202512244.
16. S. A. Mohamed, R. Zheng, N. Zhu, D. Zhao and J. Jiang, *J. Am. Chem. Soc.*, 2025, **147**, 12251-12262.
17. L. Li, L. Guo, D. H. Olson, S. Xian, Z. Zhang, Q. Yang, K. Wu, Y. Yang, Z. Bao, Q. Ren and J. Li, *Science*, 2022, **377**, 335-339.
18. X.-J. Xie, H. Zeng, Y.-L. Huang, Y. Wang, Q.-Y. Cao, W. Lu and D. Li, *Chem*, 2025, **11**.
19. Q. Liu, Y. Miao, L. F. Villalobos, S. Li, H.-Y. Chi, C. Chen, M. T. Vahdat, S. Song, D. J. Babu, J. Hao, Y. Han, M. Tsapatsis and K. V. Agrawal, *Nat. Mater.*, 2023, **22**, 1387-1393.
20. X. Wu, X. Tian, W. Zhang, X. Peng, S. Zhou, P. J. S. Buenconsejo, Y. Li, S. Xiao, J. Tao, M. Zhang and H. Yuan, *Angew. Chem. Int. Ed.*, 2024, **63**, e202410411.
21. X. Zhang, X. Tian, N. Wu, S. Zhao, Y. Qin, F. Pan, S. Yue, X. Ma, J. Qiao, W. Xu, W. Liu, J. Liu, M. Zhao, K. Ostrikov and Z. Zeng, *Sci. Adv.*, 2025, **10**, eadl6498.
22. H. Wang, Y. Liu and J. Li, *Adv. Mater.*, 2020, **32**.
23. M. Xu, S.-S. Meng, P. Cai, W.-Q. Tang, Y.-D. Yin, J. A. Powell, H.-C. Zhou and Z.-Y. Gu, *Chem. Sci.*, 2021, **12**, 4104-4110.
24. R. Lyndon, Y. Wang, I. M. Walton, Y. Ma, Y. Liu, Z. Yu, G. Zhu, S. Berens, Y.-S. Chen, S. G. Wang, S. Vasenkov, D. S. Sholl, K. S. Walton, S. H. Pang and R. P. Lively, *Chem. Commun.*, 2022, **58**, 12305-12308.
25. Q. Wang, Y. Li, Z. Qiu, D. Zhou, L. Yang, X. Suo, X. Cui and H. Xing, *Angew. Chem. Int. Ed.*, 2024, **63**, e202408817.
26. X. Cui, Z. Niu, C. Shan, L. Yang, J. Hu, Q. Wang, P. C. Lan, Y. Li, L. Wojtas, S. Ma and H. Xing, *Nat. Commun.*, 2020, **11**, 5456.
27. J. Li, B. Sheng, R. Chen, H. Wu, W. Zhou, F. Zheng, B. Liu, Q. Yang, Z. Zhang, Y. Yang, Q. Ren and Z. Bao, *Adv. Mater.*, 2025, **37**, 2413506.
28. Z. Chu, J. Li, F. Chen, Y. Cao, L. Chen, F. Zhou, H. Ma, Q. Yang, Z. Zhang, K. Qiao, Q. Ren and Z. Bao, *ACS Cent. Sci.*, 2024, **10**, 1861-1870.
29. H. Yuan, K. Li, D. Shi, H. Yang, X. Yu, W. Fan, P. J. S. Buenconsejo and D. Zhao, *Adv. Mater.*, 2023, **35**, 2211859.
30. H. Zeng, M. Xie, T. Wang, R.-J. Wei, X.-J. Xie, Y. Zhao, W. Lu and D. Li, *Nature*, 2021, **595**, 542-548.
31. L. Li, Z. Yang, Q. Wang, L. Yang, X. Suo, X. Cui and H. Xing, *Small*, 2025, **21**, 2412724.
32. M.-Y. Zhou, X.-W. Zhang, H. Yi, Z.-S. Wang, D.-D. Zhou, R.-B. Lin, J.-P. Zhang and X.-M. Chen, *J. Am. Chem. Soc.*, 2024, **146**, 12969-12975.
33. Z.-J. Jiang, Y. Wang, D. Luo, R.-J. Wei, W. Lu and D. Li, *Angew. Chem. Int. Ed.*, 2024, **63**, e202403209.
34. X.-W. Zhang, H. He, Y.-W. Gan, Y. Wang, N.-Y. Huang, P.-Q. Liao, J.-P. Zhang and X.-M. Chen, *Angew. Chem. Int. Ed.*, 2024, **63**, e202317648.
35. F. Xie, L. Chen, E. M. Cedeño Morales, S. Ullah, Y. Fu, T. Thonhauser, K. Tan, Z. Bao and J. Li, *Nat. Commun.*, 2024, **15**, 2240.
36. S. Grimme, S. Ehrlich and L. Goerigk, *J. Comput. Chem.*, 2011, **32**, 1456-1465.
37. G. Kresse and J. Furthmüller, *Phys. Rev. B*, 1996, **54**, 11169-11186.
38. M. Krüger, R. Siegel, A. Dreischarf, H. Reinsch, J. Senker and N. Stock, *Micropor. Mesopor. Mat.*, 2015, **216**, 27-35.
39. G. M. R. Dontireddy, S. P. Suman, J. L. Merino-Gardea, A. H. Javed, J. Wang, T. Chen, S. Kampouri and H. Banda, *J. Mater. Chem. A*, 2025, **13**, 8734-8741.
40. L. Yan, H.-T. Zheng, L. Song, Z.-W. Wei, J.-J. Jiang and C.-Y. Su, *Chem. Eng. J.*, 2023, **472**, 145145.
41. A. Gładysiak, A.-Y. Song, R. Vismara, M. Waite, N. M. Alghoraibi, A. H. Alahmed, M. Younes, H. Huang, J. A. Reimer and K. C. Stylianou, *JACS Au*, 2024, **4**, 4527-4536.
42. M. Lammert, H. Reinsch, C. A. Murray, M. T. Wharmby, H. Terraschke and N. Stock, *Dalton Trans.*, 2016, **45**, 18822-18826.
43. Y. Yang, P. Bai and X. Guo, *Ind. Eng. Chem. Res.*, 2017, **56**, 14725-14753.



The data supporting this article have been included as part of the Supplementary Information.

